

We are IntechOpen, the world's leading publisher of Open Access books Built by scientists, for scientists

6,900

Open access books available

186,000

International authors and editors

200M

Downloads

Our authors are among the

154

Countries delivered to

TOP 1%

most cited scientists

12.2%

Contributors from top 500 universities



WEB OF SCIENCE™

Selection of our books indexed in the Book Citation Index
in Web of Science™ Core Collection (BKCI)

Interested in publishing with us?
Contact book.department@intechopen.com

Numbers displayed above are based on latest data collected.
For more information visit www.intechopen.com



Methods for Blind Estimation of Speckle Variance in SAR Images: Simulation Results and Verification for Real-Life Data

Sergey Abramov, Victoriya Abramova,
Vladimir Lukin, Nikolay Ponomarenko, Benoit Vozel,
Kacem Chehdi, Karen Egiazarian and Jaakko Astola

Additional information is available at the end of the chapter

<http://dx.doi.org/10.5772/57040>

1. Introduction

Blind estimation of noise characteristics (BENC), such as noise type, its statistics and spectrum, has become an actual practical task for various image processing applications (Vozel et al., 2009). There are several reasons for this. First, noise is one of the main factors degrading and determining the quality of images of different types: grayscale and color optical (Liu et al., 2008; Foi et al., 2007; Plataniotis&Venetsanopoulos, 2000), component images in certain sub-bands of hyperspectral remote sensing data (Aiazzi et al., 2006), radar and ultrasound medical images (Lin et al., 2010; Oliver&Quegan, 2004), etc. Second, information on noise characteristics is valuable and widely exploited in most of stages of image processing. For example, it is used in edge detection for threshold setting (Davies, 2000), image filtering (Touzi, 2002; Lee et al., 2009) including denoising techniques based on orthogonal transforms (Mallat, 1998; Sendur&Selesnick, 2002; Egiazarian et al., 1999), image reconstruction (Katsaggelos, 1991), lossy compression of noisy images (Bekhtin, 2011), non-reference assessment of image visual quality (Choi et al., 2009), etc. Third, although there can be initial assumptions on noise type and a range of variations of its statistical parameters, these parameters can be quite different even for a given imaging system depending upon conditions of its operation. The requirements to information accuracy on noise parameters are rather strict, e.g., variance of pure additive or pure multiplicative noise has to be known or pre-estimated with a relative error not larger than $\pm 20\%$ (Abramov et al., 2004). Thus, it is often desirable to estimate noise characteristics for a given image.

Besides, amount of images offered by various imaging systems increases enormously. Therefore, it becomes difficult to evaluate noise characteristics in an interactive manner since this requires time, perfect skills, and availability of the corresponding software. Moreover, there are practical situations and applications for which it is impossible to find a highly qualified expert to perform the task of evaluation of the noise characteristics. The examples are estimation of noise characteristics in remote sensing images on-board satellites (Van Zyl et al., 2009). BENC can be also useful even if an expert is involved to analysis of the noise characteristics. This happens, e.g., if a newly designed and manufactured imaging system is verified to check do the main properties of the noise present in the formed images conform expected (forecasted) ones. Then, the output estimates of BENC can be compared to the outcomes of the expert analysis and support (control) each other.

There are quite many known methods of BENC designed so far. A few of them can operate on images corrupted by a general type of signal-dependent noise (Liu et al., 2008). Most of known BENC methods are able to deal only with a particular type of noise under assumption that the noise type is known a priori or pre-determined in an automatic manner (Vozel et al., 2009). The case of pure additive noise has been studied more thoroughly in literature (see Vozel et al. 2009; Zoran&Weiss, 2009; Abramov et al., 2008; Lukin et al. 2007, and references therein). Some of these methods can be, after certain modifications, applied to estimation of multiplicative noise variance. These modifications basically relate to either application of logarithmic type homomorphic transform or a special approach to form local estimates of multiplicative noise relative variance as a normalization of local variance estimates by squared local mean (Vozel et al. 2009). However, quite many BENC methods exploit local estimate scatter-plots and line (curve) fitting into them to evaluate multiplicative noise variance (Lee et al., 1992; Ramponi&d'Alvise, 1999). Note that a multiplicative noise is typical for radar imagery, in particular, images acquired by synthetic aperture radars (SARs) where coherent principles of image forming are employed (Solbo&Eltoft, 2004; Oliver&Quegan, 2004). Speckle is a specific noise-like phenomenon arising in formed images and it is known to be the dominant factor degrading their quality (Oliver&Quegan, 2004). For many operations of radar (and ultrasound) image processing, the characteristics of the speckle are to be known in advance or pre-estimated (Lee et al., 2009; Solbo&Eltoft, 2008).

One can argue that there are many practical situations when speckle characteristics such as the (relative) variance of the multiplicative noise (or the efficient number of looks) and the speckle distribution law are known in advance or can be predicted from theory (Oliver&Quegan, 2004). This holds if a given SAR operates in a known mode (e.g. forms one-look amplitude images) and the operation parameters are stable. Then, it is enough to carry out a preliminary analysis of several images acquired by this SAR manually (in interactive mode) to be sure that the aforementioned characteristics (parameters) conform theory and are stable enough.

However, in many practical situations, it is worth applying BENC, sometimes in addition to an interactive analysis. First, suppose that a new SAR is tested and it is desirable to know whether or not it provides the desired (forecasted, expected) characteristics. Second, one might deal with SAR images for which full description of the imaging mode used is absent (Lee et

al., 1992; Ramponi&d'Alvise, 1999). Third, although it is assumed that the multi-look mode of image formation allows decreasing the speckle variance by the number of looks, this is not absolutely true and, in practice, noise reduction is not as efficient as ideally predicted (Anfinssen et al., 2009; Foucher et al., 2000).

Therefore, two important questions arise: what is the accuracy of the existing blind estimation methods and what BENC to apply? To our best knowledge, there are no studies dealing with intensive testing of BENC with application to speckle (our conference paper (Lukin et al., 2011) seems to be one of the first attempts in this direction). By intensive testing we mean the use of tens of different images having different content and/or many realizations of speckle for both single and multi-look modes. There are several reasons why such testing has not been carried out yet. The main reason is the absence of the test radar images commonly accepted by the radar data processing community. We have to stress here that it is quite difficult to create test SAR images since one has to find an answer to many particular questions as what terrain and objects to simulate, what model of the carrier trajectory and its instabilities to use, to consider moving objects or not, what is SNR in radar receiver input, what kind of received signal processing is used (Dogan&Kartal, 2010; Di Martino et al., 2012), etc. Another reason is that, maybe, designers of BENC for speckle have been satisfied by accuracy of the obtained estimates for a limited set of processed images and have not tried applying their methods to a wider variety of data.

Experience obtained recently in testing BENCs for additive and signal dependent noise cases (Vozel et al., 2009; Abramov et al., 2011; Lukin et al., 2009b) clearly demonstrates the following. First, whilst a given method can produce an acceptable accuracy for many tested images, there can be a few test images (usually highly textural ones and/or with clipping effects) for which abnormal (unacceptable) estimates are obtained. Just to these images one has to pay more attention in attempts to improve a methods' performance. Second, a spatial correlation of noise present in most of real life images and often ignored in a design and testing of many BENC techniques can considerably influence an accuracy of estimation methods (Abramov et al., 2008). Recall that a spatial correlation of speckle is a feature typical for SAR images (Solbo&Eltoft, 2008, Lukin et al., 2008; Lukin et al., 2009; Ponomarenko et al., 2011) which is not often taken into account in SAR image simulations.

Thus, we come to a necessity to perform intensive testing of BENC methods without having a set of standard test images. Our idea then is to create a set of test SAR images with a priori known characteristics of the speckle similar to those ones observed in practice. In this sense, TerraSAR-X images can be a good choice (in Section 2, we explain this in detail). Note that quite many of them are now available in the convenient form and their amount is rapidly growing (see <http://www.infoterra.de/free-sample-data>). Then, it becomes possible to test BENCs for simulated data (Section 3) and to predict what could happen in practice. These predictions are then verified for the considered methods for high quality data provided by TerraSAR-X data (Section 4) to offer practical recommendations on the BENC method selection and setting its parameters. Finally, conclusions follow.

2. Basic properties of speckle and its modeling

Speckle is a typical example for which pure multiplicative model is usually exploited (Touzi, 2002; Oliver&Quegan, 2004). This means that a dependence of signal dependent noise variance on true value $\sigma_{sd}^2 = f(I^{tr})$ is monotonically increasing proportionally to squared (true value). Speckle is not Gaussian and its probability density function (PDF) depends upon a way of image forming (amplitude or intensity) and number of looks (Oliver&Quegan, 2004). PDF of the speckle considerably differs from Gaussian if a single-look imaging mode is used and it is either Rayleigh (for amplitude images) or negative exponential (for intensity images) for the case of fully developed speckle. If multi-look imaging mode is applied, the speckle PDF becomes closer to Gaussian and depends upon the number of looks.

To get an imagination on fully developed speckle PDF, consider real-life data produced by TerraSAR-X imager. Its attractive feature is that data (images) are freely available at the aforementioned site. These data have full description of parameters of the imaging system operation mode used for obtaining each presented image. Large size images (thousands to thousands pixels) for many different areas of the Earth are offered. Furthermore, a brief description of a territory, observed effects and cover types is given. This allows selecting and processing data with different numbers of looks, properties of a sensed terrain, a desired polarization, etc. Fragments of certain size as 512x512 pixels can be easily cut from large size data arrays and studied more thoroughly. Another positive feature is that single-look images are presented in the complex valued form. This allows obtaining single-look images in aforementioned forms (representations). It also makes possible to analyze distributions of real and imaginary part values for image fragments, etc. While considering single-look SAR images in this paper, we use amplitude images since it is the most common form and it provides convenient representation for visual analysis.

One more advantage is that TerraSAR-X is a high quality system designed by specialists from German Aerospace Agency DLR who have large experience in creation and management of spaceborne SAR systems (Herrmann et al., 2005). The TerraSAR-X imager provides a stability of noise characteristics and practical absence of an additive noise in formed images. Later, it will be explained why this is so important for further analysis.

To partly corroborate conformity of theory and practice for single-look SAR images, we have manually cropped several sub-arrays of complex valued data that correspond to homogeneous terrain regions. The histogram of real (in-phase) part values for one such a fragment is presented in Fig. 1(a) where sample data mean is close to zero. The histogram for imaginary (quadrature) part is very similar. Gaussianity tests hold for both data sub-arrays. The histogram of the amplitude single-look image for the same fragment is represented in Fig. 1(b). Since both components of complex valued data are Gaussian with approximately the same variance, the amplitude values obey Rayleigh distribution. This one more time shows that for single-look amplitude images speckle can be simulated as pure multiplicative noise having Rayleigh PDF. Using modern simulation tools as, e.g., Matlab, this can be done easily, at least, for the case of independent identically distributed (i.i.d.), i.e. spatially uncorrelated speckle.

The histogram in Fig. 1(b) also shows one more aspect important for simulations. Speckle image values can be by 3...4 times larger than mean (which is close to I^{tr} in homogeneous image regions). Then, if the values of I^{tr} are modelled as 8-bit data, the noisy values can be outside the limits 0...255 and, therefore, 16-bit representation of a simulated noisy image is to be used to preserve statistics of the speckle. In Section 3, we will show what might happen to the estimates provided by BENCs if clipping effects take place for simulated noisy SAR images, i.e. if they are represented as 8-bit data.

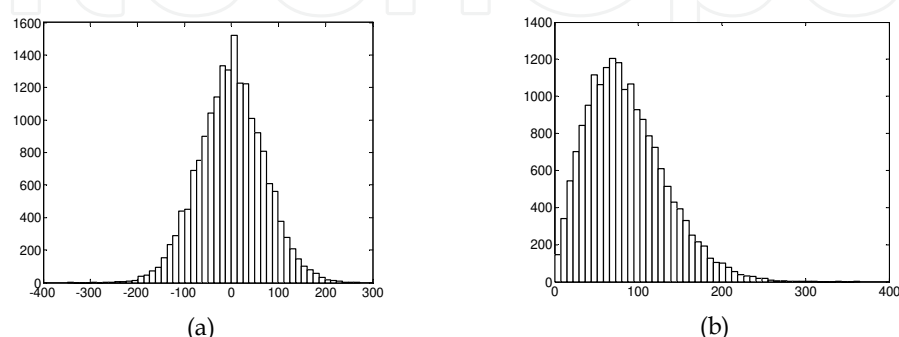


Figure 1. Histograms of distributions for in-phase component (a) and amplitude (b) of complex-valued data in image homogeneous region

To additionally analyze statistics of the speckle, we have also tested several manually cropped homogeneous regions in different single-look images that correspond to either rather large (about 70x70 pixels) agricultural fields and water surface. The estimated speckle variance $\hat{\sigma}_{\mu}^2 = \sum_{G_{hom}} (I_{ij} - \hat{I}_{G_{mean}})^2 / \hat{I}_{G_{mean}}^2$, $\hat{I}_{G_{mean}} = \sum_{G_{hom}} I_{ij}$ (I_{ij} is an ij -th image pixel, G_{hom} is a selected homogeneous region) has varied from 0.265 to 0.285. This is in a good agreement with a theoretically stated $\sigma_{\mu}^2 = 0.273$ for Rayleigh distributed speckle in amplitude single-look SAR images. Higher order moments (skewness and kurtosis) for the studied homogeneous image regions are also in appropriate agreement with the theory (Oliver&Quegan, 2004). This means that for both simulated and real-life single-look amplitude SAR images any BENC should provide estimates of speckle variance close enough to 0.273.

To consider and simulate speckle more adequately, we have also analyzed spatial correlation of speckle using TerraSAR-X data. This has been done in three different ways. First, standard 2D autocorrelation function (ACF) estimates have been obtained for 32x32 pixels size homogeneous fragments. They have been inspected visually and have demonstrated the absence of far correlation and the presence of essential correlation for neighboring pixels in single-look amplitude images (see example in Fig. 2(a)). It is interesting that even higher correlation for neighboring pixels has been observed for multi-look images (see example in Fig. 2(b)). There are also ACF side lobes for azimuth direction that, most probably, arise due to peculiarities of the SAR response to a point target.

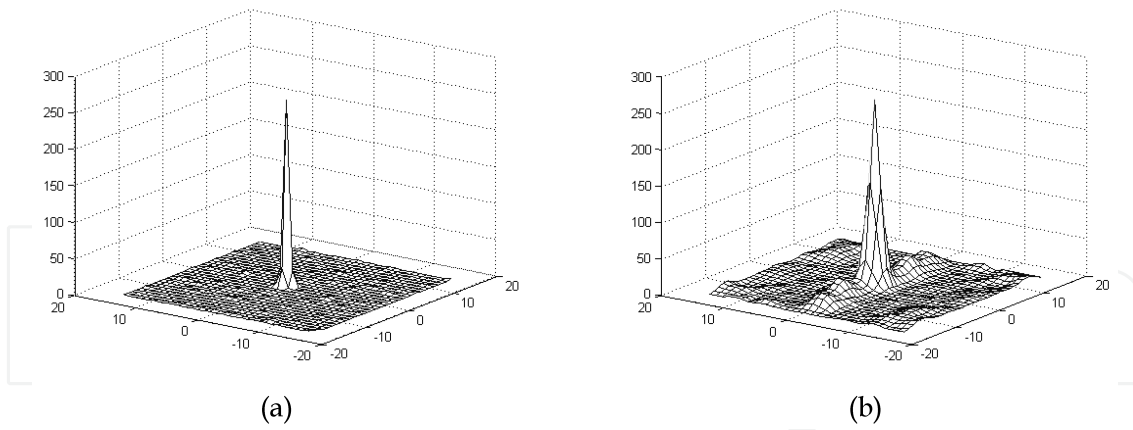


Figure 2. ACF estimates for 32x32 pixel homogeneous fragments in single-look (a) and multi-look (b) TerraSAR-X images

Second, we have analyzed a normalized 8x8 DCT spectrum estimates obtained in a blind manner (Ponomarenko et al., 2010) for several considered images. These estimates also clearly indicate that speckle is spatially correlated, i.e., not i.i.d. (Lukin et al., 2011).

Third, we have also calculated a parameter r (Uss et al., 2012) able to indicate spatial correlation of noise for any type of signal dependent noise with spatially stationary spectral characteristics. For determination of r , two local estimates of noise variance are derived for each 8x8 pixel block with its left upper corner defined by indices l and m . The first estimate is calculated in the spatial domain

$$\hat{\sigma}_{lm}^2 = \sum_{i=l}^{l+7} \sum_{j=m}^{m+7} (I_{ij} - \hat{I}_{lm})^2 / 63, \quad \hat{I}_{lm} = \sum_{i=l}^{l+7} \sum_{j=m}^{m+7} I_{ij} / 64, \quad (1)$$

and the second estimate is calculated in the DCT domain as

$$(\hat{\sigma}_{lm}^{sp})^2 = (1.483 \text{med}(|D_{qs}^{lm}|))^2 \quad (2)$$

where D_{qs}^{lm} , $q=0, \dots, 7$, $s=0, \dots, 7$ except $q=s=0$ are DCT coefficients of lm -th block of a given image. Then, the ratio $R_{lm} = \hat{\sigma}_{lm} / \hat{\sigma}_{lm}^{sp}$ is calculated for each block. After this, the histogram of these ratios for all blocks is formed and its mode r is determined by the method (Lukin et al., 2007). For all considered real-life SAR images, the value of r was larger than 1.05 (Lukin et al., 2011b) for single-look SAR images and considerably larger for multi-look ones. This additionally gives an evidence in favor of the hypothesis that speckle is spatially correlated. Thus, we can state that speckle is spatially correlated in the considered TerraSAR-X images, both single- and multi-look ones. Then, this effect should be taken into account in simulations.

To simulate single- and multi-look SAR images, we have used four aerial optical images as I^{tr} (all test images are of size 512x512pixels). These four images are presented in Fig. 3. Positive features of these images allowing to use them in simulation of SAR data are the following.

First, these images have practically no self-noise that could later influence blind estimation of speckle statistics.

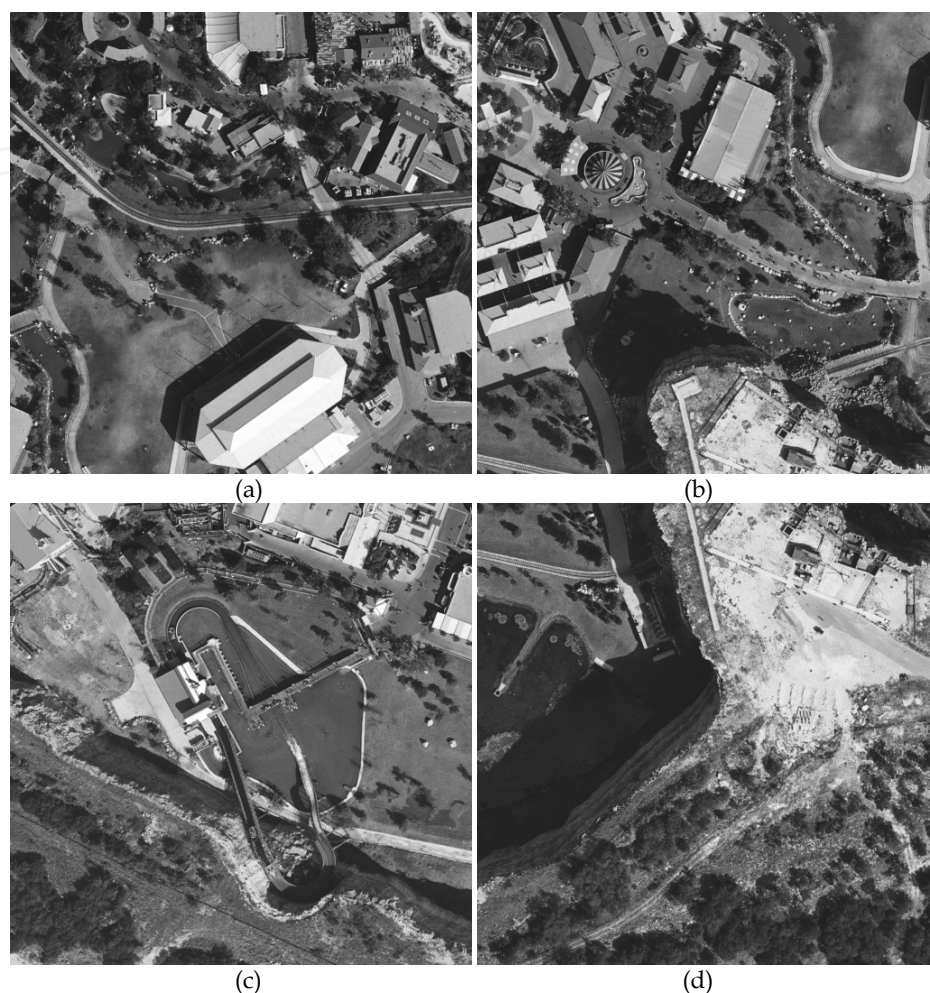


Figure 3. Noise-free (true) test images used for simulating SAR images

Second, these are the images of natural scenes and, thus, they contain large quasi-homogeneous regions, edges with different contrasts, various textures and small-sized targets.

Note that we have simulated speckle with the same statistics for all pixels ignoring the fact that for small-sized targets it might differ from speckle in homogeneous image regions. This simplification is explained by the following two reasons. First, more complicated models of speckle are required for small-sized targets. Second, the percentage of pixels occupied by small-sized targets is quite small in real-life images (Lee et al., 2009) and local estimates of noise statistics in the corresponding scanning windows are anyway abnormal. Thus, these local estimates are “ignored” by the BENCs considered below which are robust (see Section 3 for more details).

Fig. 4 gives two examples of noisy test image with fully developed speckle (single look). For one of them (Fig. 4(a)) speckle is i.i.d. whilst for the second (Fig. 4(b)) speckle is spatially

correlated (see details of its simulation below). Even visual analysis of these two noisy images allows noticing the difference in speckle spatial correlation. As it will become clear from the visual analysis of real-life SAR images presented later in Section 4, the case shown in Fig. 4(b) is much closer to practice.

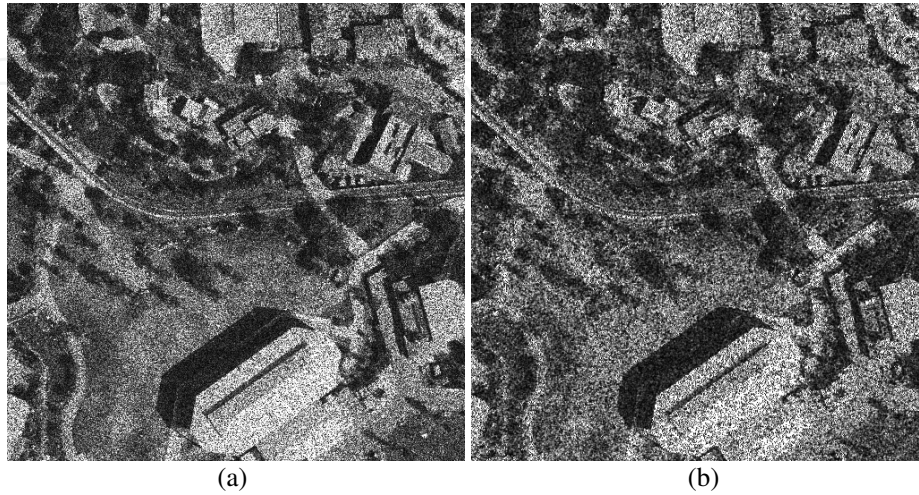


Figure 4. The first test image corrupted by i.i.d. (a) and spatially correlated (b) speckle

Thus, from a practical point of view, it is more reasonable to simulate spatially correlated speckle. This can be done in different ways. In our study, we have employed the following simulation algorithm:

1. Generate 2D array of a required size $I_{\text{Im}} \times J_{\text{Im}}$ for Gaussian zero mean spatially correlated noise (GCN – Gaussian correlated noise) with a desired spatial spectrum (this is a standard task solution of which is omitted).
2. Transform the 2D GCN data array into 1D array C of size $K = I_{\text{Im}} \times J_{\text{Im}}$ in a pre-selected way, e.g., by row-by-row scanning.
3. Generate 1D array B of i.i.d. Rayleigh distributed unity mean random variables of size $K = I_{\text{Im}} \times J_{\text{Im}}$.
4. For the array C , form an array of indices CI in such a manner that $CI(1)$ is the index of the element in C which is the largest, $CI(2)$ is the index of the element in C which is the second largest, and so on. Finally, $CI(K)$ is the last element of the array CI which is the index of the smallest element of C .
5. Similarly, form an index array BI for the array B .
6. For $k=1..K$ make valid the condition $C(CI(i))=B(BI(i))$. Then, noise with Gaussian distribution is replaced by noise with the required distribution (Rayleigh in our case).
7. The obtained array C is transformed to 2D array RES of size $K = I_{\text{Im}} \times J_{\text{Im}}$ in the way inverse to it has been done in step 2.

The source code in Matlab that realizes the described algorithm is presented below:

```
C=GCN(:);
B=random('rayleigh',1,1,M*N)/1.26;
[CC,CI]=sort(C);
[BB,BI]=sort(B);
C(CI)=B(BI);
RES=reshape(C,M,N);
```

Here M, N correspond to I_{Im} and J_{Im} (that is to the simulated image size), and all other notations are the same as described above. The obtained 2D array has a Rayleigh distribution and has practically the same spatial correlation properties as GCN. Then the values of $\text{RES}(i,j)$ are pixel-wise multiplied by I_{ij}^{true} to obtain the corresponding speckle values I_{ij}^n , $i=1, \dots, I_{\text{Im}}, j=1, \dots, J_{\text{Im}}$.

The image presented in Fig. 4(b) has been obtained in the way described above. Moreover, this allows getting multi-look images if several realizations of the speckle with desired spectrum are generated and then averaged.

3. Considered blind estimation techniques and their accuracy analysis for simulated data

Describing the considered BENC methods, one should keep in mind that blind estimates of speckle characteristics obtained for a given method can differ from each other due to the following factors:

- properties and parameters (if they can be varied or user defined) of a method applied;
- method robustness with respect to outliers;
- content of an analyzed image;
- an observed speckle realization in the considered image;
- clipping effects (if they take place).

Because of this, we first describe BENCs used in our studies and the main principles put into their basis. Then, simulation results are presented for simulated single- and multi-look SAR images, and the analysis of these results is performed.

3.1. Considered BENCs

As it has been mentioned in Introduction, there are two basic approaches to blind estimation of σ_{μ}^2 . The first approach presumes forming local estimates of speckle variance and robust

processing of the obtained local estimates. The second approach is based on obtaining a scatter-plot and robust regression line fitting into it.

Let us start from considering the former approach. It consists of the following stages. At the first stage, an analyzed image is divided into non-overlapping or overlapping blocks and local estimates are obtained as

$$\hat{\sigma}_{\mu\ lm}^2 = \sum_{i=l}^{l+N-1} \sum_{j=m}^{m+N-1} (I_{ij} - \hat{I}_{lm})^2 / ((N^2 - 1) \hat{I}_{lm}^2), \quad \hat{I}_{lm} = \sum_{i=l}^{l+N-1} \sum_{j=m}^{m+N-1} I_{ij} / N^2, \quad (3)$$

where N denotes the block size under assumption that it has a square shape. According to a previous experience (Abramov et al., 2008), N is recommended to be from 5 till 9; $N=5$ is usually enough for i.i.d. noise whilst it is better to set N equal to 7, 8 or 9 for spatially correlated noise.

To understand the operation principles of the first group of methods, it can be useful to look at distributions of the local estimates (3). As examples, the two distributions of local estimates $\hat{\sigma}_{\mu\ lm}^2$ for the two real-life (TerraSAR-X) single-look elementary images (presented in Fig. 5(a) and Fig. 5(b)) are shown in Figs. 6(a) and 6(b), respectively ($N=7$ and non-overlapping blocks are used). It is easy to see that both distributions characterized by histograms have modes close to 0.273. Meanwhile, the percentages of “normal” local estimates (3) that produce quasi-Gaussian parts of distributions are considerably different – look at maximal values in histograms. Suppose that normal local estimates are those ones smaller than 0.5. Then, the probability p of occurrence of “normal” local estimates is approximately equal to 0.6 for the histogram in Fig. 6(a) and to 0.9 for the histogram in Fig. 6(b). For other tested real-life single-look images (in particular, those ones shown in Fig. 7(a) and 7(b)), the estimated values of p are from 0.55 till 0.9. The same holds for the simulated test images presented in the previous Section.

Besides, the distributions in Fig. 6 differ by heaviness of the right-hand tail. Recall that this tail stems from the presence of the so-called “abnormal” local estimates (3) that are obtained in heterogeneous image blocks (Vozel et al., 2009). For the elementary images that have a simpler structure (Figures 5(b) and 7), the tail heaviness is considerably less (see Fig. 7(b)).

The property that the distributions have maxima with the mode close to the true value of σ_{μ}^2 has been put into the basis of several BENC methods for estimation of noise variance (Vozel et al., 2009). The task is then to find the distribution mode automatically, robustly and with a high enough accuracy. For this purpose, it is possible to exploit robust mode finders such as a sample myriad, bootstrapping and minimal inter-quantile distance with properly (adaptively) set parameters. Since an improved minimal inter-quantile distance estimator provides the best accuracy (Lukin et al., 2007), we use it in our further studies. The technique based on obtaining the set of local estimates according to (3) and estimation of its mode by the improved minimal inter-quantile distance estimator (Lukin et al., 2007) is further referred as **Method 1**. A variable parameter of this method is the block size.

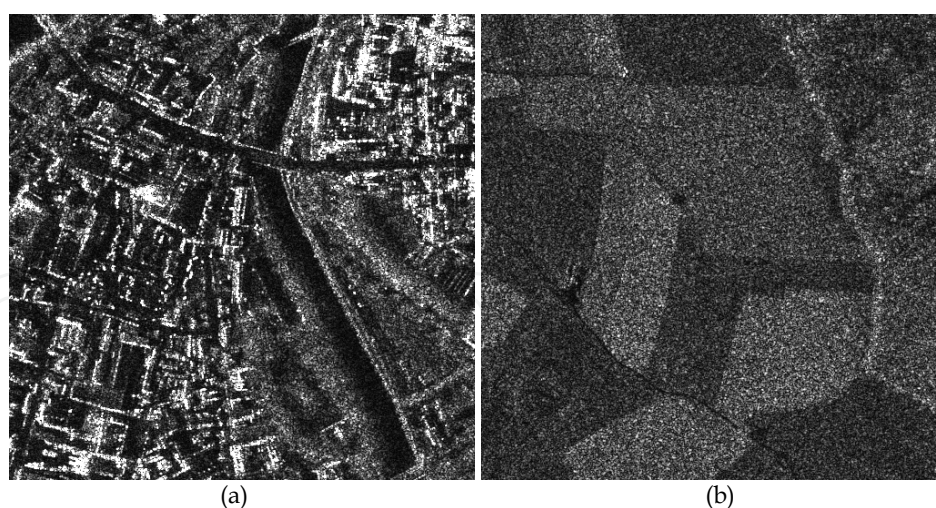


Figure 5. Two elementary single look amplitude SAR images for Rosenheim region

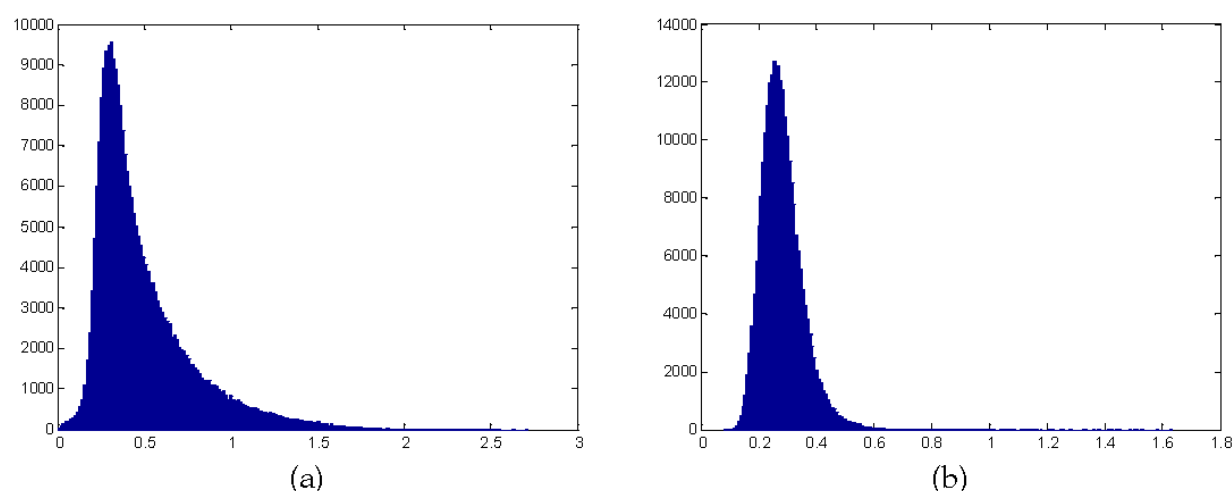


Figure 6. Histograms of local estimates (3) for the elementary images in Fig. 5(a) and Fig. 5(b)

The second group of BENC methods, as it has been mentioned above, is based on scatter-plots. A traditional way of scatter-plot representation for signal-dependent noise is the following. For each block, a point in Cartesian system is obtained where its Y coordinate corresponds to a local variance estimate $Y = \hat{\sigma}_{loc}^2$ and a local mean estimate is its argument (X axis coordinate $X = \bar{I}_{loc}$). An example of such a scatter-plot for the image in Fig. 5(b) is presented in Fig. 8(a). A curve $\hat{\sigma}_{loc}^2 = \sigma_{\mu}^2 \bar{I}_{loc}$ is depicted in this scatter-plot. It is seen that it goes through the centers of the main clusters of this scatter-plot (the cluster centers are indicated by red squares) where the clusters are formed by normal local estimates (see details below). However, there are also quite many points that are located far away from this curve and cluster centers. These points correspond to abnormal local estimates obtained in heterogeneous blocks. This means that if one presumes to fit a polynomial type curve $\hat{\sigma}_{loc}^2 = D \bar{I}_{loc}$ and then to obtain $\hat{\sigma}_{\mu}^2 = D$, where D is

the parameter of the fitted curve, the method of curve fitting should be robust with respect to outliers.

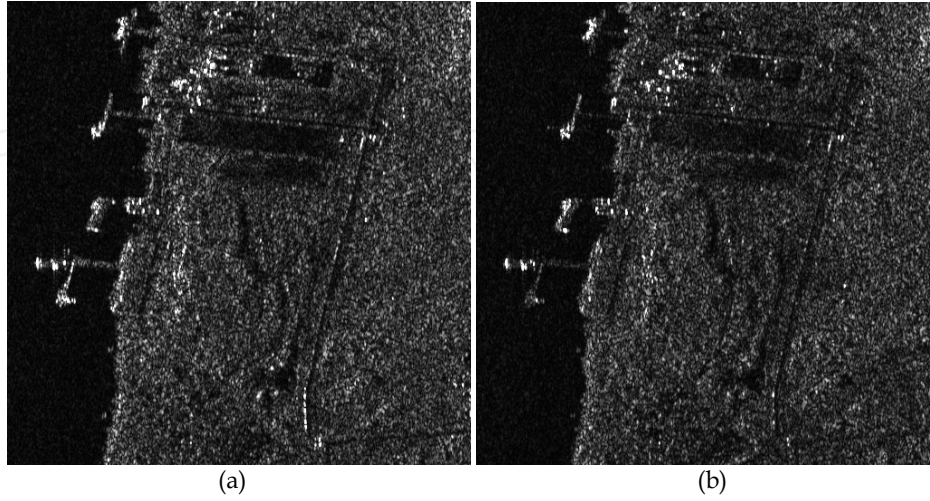


Figure 7. The 512x512 pixels elementary single-look amplitude SAR images of Indonesia for (a) HH and (b) VV polarizations

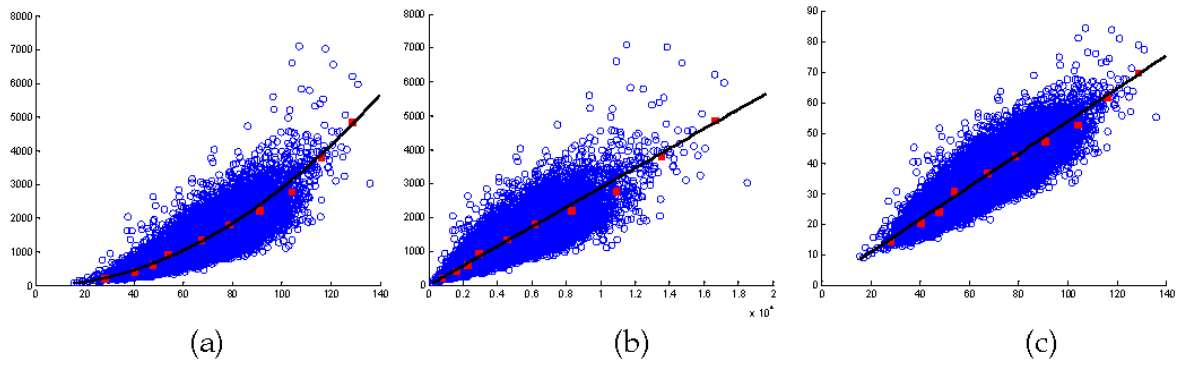


Figure 8. Different types of scatter-plots for the image in Fig. 5(b)

There are also other ways to obtain a scatter-plot. One variant is that a point Y coordinate corresponds to a local variance estimate $Y = \hat{\sigma}_{loc}^2$ and a squared local mean estimate is its argument (X axis coordinate $X = \bar{I}_{loc}^2$). An example of such a scatter-plot obtained for the same single-look image is represented in Fig. 8(b). Then one has to fit a curve

$$\hat{\sigma}_{loc}^2 = E \bar{I}_{loc}^2 \quad (4)$$

i.e. straight line where the estimate $\hat{\sigma}_{loc}^2 = E$, E is the parameter of the fitted line. Another option is to obtain a scatter-plot in such a way that a point coordinate Y relates to a local standard deviation estimate $Y = \hat{\sigma}_{loc}$ where its argument (X axis coordinate $X = \bar{I}_{loc}$) is the corresponding

local mean estimate. Then one has $\hat{\sigma}_{loc} = F \bar{I}_{loc}$ where F is the fitted straight line parameter that serves as the estimate $\hat{\sigma}_{\mu}$. This kind of a scatter-plot is shown in Fig. 8(c) for the same single-look SAR image. Visual analysis of the scatter-plots in Figs. 8(b) and 8(c) shows that for them there are also some clusters of normal local estimates whereas abnormal estimates are present as well. An advantage of the latter two approaches is that it is, in general, simpler to fit a straight line than a higher order polynomial. In particular, there are standard means for this purpose as, e.g., the Matlab version of robustfit method (DuMouchel&O'Brien, 1989). For methods analyzed below, we have used the approach based on (6).

Finally, there are also methods that exploit scatter-plot data to find cluster centers and curve (line) fitting using these scatter-plot centers (Zabrodina et al., 2011; Abramov et al., 2011). Cluster centers are indicated by red color dots in scatter-plots in Fig. 8. The cluster center coordinates relate to $Y_q = \hat{\sigma}_{norm\ q}^2$, $X_q = \hat{I}_{norm\ q}$, $q=1, \dots, Q_{cl}$ where $\hat{\sigma}_{norm\ q}^2$ is the estimate of distribution mode of local variance estimates for a q -th cluster basically based on normal local estimates, $\hat{I}_{norm\ q}$ denotes the estimate of distribution mode of the local mean estimates for this cluster, and Q_{cl} is the number of clusters. Clusters are obtained by a simple division of the scatter-plot horizontal axis to a fixed number of intervals (we recommend to use ten intervals). The estimates of distribution modes for each cluster are obtained by the improved minimal inter-quantile distance estimator (Lukin et al., 2007).

There is the straight line fitted into the cluster centers in Figs. 8(b) and 8(c). In this case, robustness with respect to abnormal local estimates is provided indirectly due to robust methods used for finding cluster centers. However, there can be also abnormal cluster centers. To reduce their influence, special techniques as RANSAC or double weighting (DW) LMSE fit can be applied (Zabrodina et al., 2011). Taking into account the comparison results (Abramov et al., 2011; Zabrodina et al., 2011), below we consider only the DW curve fitting to scatter-plot since this method, on the average, provides the best results. It is possible to use different sizes of blocks for local variance and local mean estimation in blocks. Below we study 5x5 and 7x7 pixel blocks. The technique based on forming a scatter-plot, its division into fixed number of clusters, finding cluster centers using mode estimation and DW line fitting is referred below as **Method 2**.

There are also other techniques based on curve fitting into cluster centers with improved robustness with respect to outliers. First, cluster centers can be determined without image pre-segmentation (as for the **Method 2** described above) and with pre-segmentation and further processing of the obtained segmentation map (Lukin et al., 2010). The result of image pre-segmentation is used in two ways. First, the number of image segments gives the number of clusters in the scatter-plot in a straightforward manner. Second, this information used for further image block discrimination into (probably) homogeneous and heterogeneous (Abramov et al., 2008; Lukin et al., 2010) allows diminishing the influence of abnormal errors on coordinate estimation of cluster centers. The next stages of the processing procedure are almost the same as in **Method 2**. However, **Method 3** also takes into account that the position of the last cluster(s) (the rightmost one(s)) can be erroneous due to clipping effects. They act so that the corresponding local estimates occur smaller than they should be in the case of

clipping absence. Then, an approach to improve estimation accuracy is to reject the rightmost cluster center(s) from further consideration. A practical rule for cluster rejection can be the following: if $\bar{I}_{norm\ q} > \max(I_{ij})/4$, $i=1, \dots, I_{lm}$, $j=1, \dots, J_{lm}$, then this cluster has to be rejected. This rule takes into account the fact that for Rayleigh distribution a random variable can be, with a small probability, by 3...4 times larger than the distribution mean.

3.2. Analysis of simulation results

Let us analyze the obtained simulation results. The main properties and accuracy characteristics of the aforementioned methods based on finding a distribution mode have been intensively studied for the case of additive noise (Lukin et al., 2007). Although the multiplicative noise case is considered here, the conclusions drawn for the additive case might be still valid for **Method 1**. Recall that one of the main conclusions drawn in (Lukin et al., 2007) is that the final blind estimate of noise variance $\hat{\sigma}_{fin}^2$ can be biased where the bias is mostly positive (i.e., the estimates are larger than the true value). The absolute value of bias is larger for images with more complex structure for which the parameter p introduced above is smaller.

Another conclusion is that the estimation bias (denoted as Δ_μ for the multiplicative noise case) usually contributes more to aggregate error $\varepsilon^2 = \Delta_\mu^2 + \theta_\mu^2$, where θ_μ^2 denotes the variance of blind estimation of σ_μ^2 . Here $\Delta_\mu = |\langle \hat{\sigma}_\mu^2 \rangle - \sigma_\mu^2|$ and $\theta_\mu^2 = \langle (\hat{\sigma}_\mu^2 - \langle \hat{\sigma}_\mu^2 \rangle)^2 \rangle$ where notation $\langle \bullet \rangle$ means averaging by realizations.

Let us check are these conclusions valid for the multiplicative noise case. Usually variance θ_μ^2 is determined for a large number of realizations of the artificially added noise that corrupts a given test noise-free image. Thus, we have simulated 200 realizations of i.i.d. speckle with Rayleigh distribution. The obtained simulation results are presented in Table 1. Analysis shows that estimation bias is also positive for all four test images and for both studied sizes of blocks. The values of θ_μ^2 are of the order 10^{-6} . Thus, they are two magnitude order less than squared bias and have negligible contribution to ε^2 . This shows that, in fact, it is possible to analyze only the estimation bias or even the estimates obtained for only one realization of the speckle. At least, this is possible for the test images of the considered size of 512x512 pixels or larger (θ_μ^2 decreases if a processed image size increases).

One more conclusion that follows from data analysis for **Method 1** in Table 1 is that the use of the block size 7x7 leads to more biased and, on the average, larger estimates than if 5x5 blocks are used. Nevertheless, the estimates for the fully developed speckle with $\sigma_\mu^2 = 0.273$ are within the required limits (Vozel et al., 2009) from $0.8 \times 0.273 = 0.218$ to $1.2 \times 0.273 = 0.328$ with high probability (it is equal to $\Delta_\mu \leq 0.055$).

Consider now data for **Method 2**. They are, mostly, more biased than for **Method 1** for the same test image and block size (see data in Table 1). Moreover, the values of θ_μ^2 and, thus, ε^2 are also sufficiently larger. However, estimation accuracy is still mainly determined by the estimation bias and, therefore, it is possible to consider only one realization of the speckle in

Method	5x5 overlapping blocks			7x7 overlapping blocks		
	Δ_μ	$\theta_\mu^2 \cdot 10^{-6}$	$\epsilon^2 \cdot 10^{-4}$	Δ_μ	$\theta_\mu^2 \cdot 10^{-6}$	$\epsilon^2 \cdot 10^{-4}$
Image Fr01						
Method 1	0.017	1.39	2.95	0.031	2.05	9.47
Method 2	0.034	19.46	11.71	0.042	20.64	17.53
Method 3	-0.008	48.17	1.06	-0.003	53.07	0.60
Image Fr02						
Method 1	0.015	1.48	2.23	0.028	1.96	7.41
Method 2	0.030	10.60	8.99	0.042	9.99	17.58
Method 3	-0.008	57.63	1.27	-0.003	42.87	0.50
Image Fr03						
Method 1	0.014	1.05	1.90	0.027	1.35	7.31
Method 2	0.032	16.01	10.49	0.045	8.51	19.93
Method 3	-0.010	31.94	1.31	-0.003	34.08	0.41
Image Fr04						
Method 1	0.012	1.04	1.47	0.025	1.22	6.25
Method 2	0.016	50.39	3.11	0.017	33.40	3.30
Method 3	0.001	23.49	0.24	0.011	28.63	1.39

Table 1. Accuracy data for the considered test images corrupted by i.i.d. speckle (single-look case)

analysis of estimation accuracy. The results for 5x5 blocks for **Method 2** are slightly better than for 7x7 pixel blocks. Hence, the use of 5x5 pixel blocks is the better choice for the case of i.i.d. speckle.

Finally, let us analyse data for **Method 3** (see Table 1). This method produces estimates that have very small absolute values of bias which is mostly negative for both 5x5 and 7x7 pixel blocks. The values of θ_μ^2 are smaller than for **Method 2** but larger than for **Method 1**. However, due to small bias, **Method 3** provides the smallest ϵ^2 among the studied BENCs and, thus, can be considered as the most accurate. The results for 5x5 and 7x7 block sizes are comparable and both block sizes can be recommended for practical use.

We have also obtained simulation results for 4-look test images corrupted by i.i.d. speckle (theoretical σ_μ^2 is equal to $0.273/4=0.068$). They are the following. For the first test image, estimation bias is 0.0101, 0.0100 and 0.0005 for **Method 1**, **Method 2**, and **Method 3**, respectively. The values of θ_μ^2 are equal to 0.21×10^{-6} , 2.71×10^{-6} , and 2.73×10^{-6} for these three methods. Finally, the values of ϵ^2 are 1.028×10^{-4} , 1.027×10^{-4} , and 0.030×10^{-4} , respectively. The results for other three test images are similar. Thus, we can state that **Method 3** again produces the best

accuracy and the influence of estimation variance θ_μ^2 can be ignored in further studies. One more observation is that the values of ε^2 for multi-look test images have become smaller than for single-look test images. This does not mean that accuracy has improved since, in fact, accuracy has to be characterized not by ε^2 but by ε/σ_μ^2 . In fact, accuracy characterized by ε/σ_μ^2 has the tendency to make worse if σ_μ^2 diminishes. This means that it is more difficult to accurately estimate speckle variance σ_μ^2 for multi-look SAR images than for single-look ones.

Consider now the case of spatially correlated noise. We have carried out preliminary simulations and established that estimation bias contributes considerably more than estimation variance to the ε^2 . Thus, below we present only the errors determined as the difference between the obtained estimate $\hat{\sigma}_\mu^2$ and the true value σ_μ^2 for single (only one) realization. The simulation results for single-look images are collected in Table 2.

Method	Method 1		Method 2		Method 3	
Block size	5x5	7x7	5x5	7x7	5x5	7x7
Image Fr01	-0.0097	0.0178	0.0056	0.0041	-0.0348	-0.0138
Image Fr02	-0.0107	0.0148	-0.0070	0.0282	-0.0207	-0.0206
Image Fr03	-0.0089	0.0151	-0.0059	0.0305	-0.0194	-0.0116
Image Fr04	-0.0142	0.0103	0.0019	0.0355	-0.0408	-0.0294

Table 2. The values of $\hat{\sigma}_\mu^2 - \sigma_\mu^2$ for the test single-look images corrupted by spatially correlated noise ($\sigma_\mu^2=0.273$)

An interesting observation that follows from data analysis in Table 2 is that the differences are mostly negative, at least, for 5x5 block size, i.e. speckle variance is underestimated. This can be explained as follows. One factor that influences blind estimation is distribution mode position. Normal local estimates in blocks that form this mode are mostly smaller than σ_μ^2 (Lukin et al., 2011b). Because of this, speckle variance estimates tend to smaller values for **Method 1**, cluster centers tend to smaller values for **Method 2** and **Method 3** as well. Another factor is the method robustness with respect to abnormal local estimates which are, recall, larger than normal estimates. These abnormal local estimates „draw“ the final estimates to another side, i.e. „force“ them to be larger. Thus, these two factors partly compensate each other. Since **Method 3** is more robust with respect to outliers (a large part of them is rejected due to pre-segmentation), this method provides smaller estimates $\hat{\sigma}_\mu^2$.

As it can be also seen from analysis of data in Table 2, the estimates $\hat{\sigma}_\mu^2$ for 7x7 blocks are larger than the corresponding estimates for 5x5 blocks. This is because mode position for normal local estimates shifts to right (to larger values) if the block size increases. This effects have been illustrated for spatially correlated speckle (Lukin et al., 2011b) and for spatially correlated additive noise (Abramov et al., 2008). Then, the final estimates for all BENCs also increase.

Analysis shows that it is worth using the block size 7x7 pixels for **Method 3** which is the most accurate according to simulation data.

Finally, simulation results for four-look test images corrupted by spatially correlated speckle are represented in Table 3. The data are presented as $\hat{\sigma}_{\mu}^2 - \sigma_{\mu}^2$ similarly to the previous case $\sigma_{\mu}^2 = 0.068$. Overestimation is observed for **Method 1** for all four test images and overestimation is larger for 7x7 blocks. Even larger overestimation takes place for **Method 2**, especially if 7x7 blocks are used. **Method 3** usually produces small under-estimation, the errors are, on the average, the smallest among the considered BENCs and 7x7 block size seems to be a proper choice.

Method	Method 1		Method 2		Method 3	
Block size	5x5	7x7	5x5	7x7	5x5	7x7
Image Fr01	0.0025	0.0081	0.0063	0.0104	-0.0067	-0.0070
Image Fr02	0.0009	0.0055	0.0027	0.0103	-0.0076	-0.0031
Image Fr03	0.0037	0.0099	0.0042	0.0127	-0.0075	-0.0015
Image Fr04	0.0038	0.0096	0.0004	0.0109	-0.0071	0.0013

Table 3. The values of $\hat{\sigma}_{\mu}^2 - \sigma_{\mu}^2$ for the test four-look images corrupted by spatially correlated noise ($\sigma_{\mu}^2 = 0.068$)

4. Verification results for real-life SAR images

First, we will verify our BENCs for the single-look real-life TerraSAR-X images presented in Figures 5 and 7. The obtained data will be considered in subsection 4.1. Besides, in subsection 4.2, we will verify our BENCs for multi-look SAR images of urban area in Canada (Toronto) (these images are presented later). All of them are acquired for HH polarization. As it is stated in file description, approximate number of looks is about 6. Thus, the expected $\sigma_{\mu}^2 \approx 0.273 / 6 \approx 0.045$. Similarly, assuming $\sigma_{\mu}^2 = 0.045$ for multi-look data, we can get the limits 0.036...0.054 for blind estimates that can be considered appropriate in practice. Let us keep these limits in mind in further analysis.

4.1. Verification results for single-look SAR images

Let us start from data obtained for **Method 1**. The estimates for block sizes 5x5, 7x7 and 9x9 pixels are collected in Table 4. We decided to analyse 9x9 blocks (not exploited in simulations) to understand practical tendencies and to be sure in our recommendations. Analysis shows that the estimates for 9x9 blocks are larger than for 7x7 and 5x5 blocks. Moreover, for the image in Fig. 5(a) the blind estimate is outside the desired limits. This happens because this image has complex structure and a large percentage of local estimates are abnormal. Although **Method 1** is robust with respect to outliers, its robustness is not enough to keep the blind estimate within the required limits.

Concerning other blind estimates, they all are within the required limits. For three of four real-life images, 7x7 block size is the best choice from the viewpoint of estimation accuracy.

Image presented in Figure	Block size		
	5x5	7x7	9x9
5(a)	0.292	0.322	0.348
5(b)	0.250	0.265	0.274
7(a)	0.240	0.270	0.283
7(b)	0.241	0.269	0.277

Table 4. Blind estimates of speckle variance for single-look real-life SAR images obtained by Method 1

Let us consider the results for two other BENC methods, both based on scatter-plots. Here we consider only the case of 7x7 blocks according to recommendations given in the previous Section. The estimates obtained by the **Method 2** for single-look images (Figs. 5 and 7) are, within the required limits (see data in Table 5) for three of four processed images. The only exception is again the image in Fig. 5(a), due to complexity of its structure. In general, the estimates for the **Method 2** are larger and less accurate than for the **Method 1** (see data in Table 4) for 7x7 blocks. We have the following explanation for that. It is quite difficult to provide unbiased estimates of cluster centers especially for those clusters that contain a relatively small number of points. Then, biasedness of cluster center estimates leads to final overestimation of speckle variance for **Method 2**.

Table 5 also contains blind estimates obtained by **Method 3**. All the estimates are within the required limits and they are, in general, more accurate than for other two methods. These conclusions also follow from analysis carried out by us for twenty 512x512 fragments of real-life SAR images (the data for 12 images are presented in Lukin et al., 2011b).

One more advantage of **Method 3** is that it is able to cope with image clipping effects. Note that clipping effects can arise due to limited range of image representation or incorrect scaling (Foi, 2009).

An example of such scatter-plot obtained as (6) for image with clipping effects is given in Fig. 9. Straight line shows the true position of the line to be fitted. As it is seen, there are three clusters (that correspond to large means) positions which are erroneous (vertical coordinates are considerably smaller than they should be). Although line fitting method is robust, the presence of a large percentage of such clusters can lead to essential errors in blind estimation.

4.2. Verification results for multi-look SAR images

The real-life six-look SAR images used in verification tests are given in Fig. 10. From visual inspection, the image in Fig. 10(d) seems to have more complex structures whilst other three images have quite large quasi-homogeneous regions. Let us see how this will influence blind estimates.

Image presented in Figure	Used method	
	Method 2, 7x7 blocks	Method 3, 7x7 blocks
5(a)	0.353	0.296
5(b)	0.289	0.259
7(a)	0.315	0.255
7(b)	0.315	0.266

Table 5. Blind estimates of speckle variance for single-look real-life SAR images obtained by Method 2 and Method 3

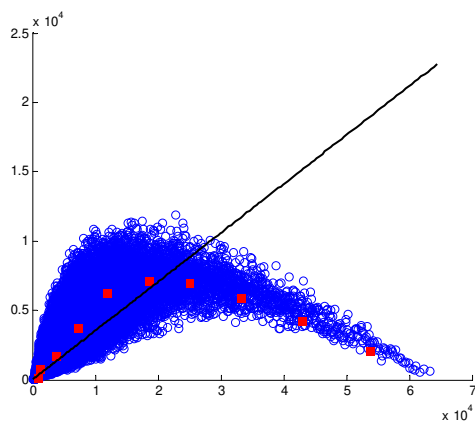


Figure 9. Scatter-plot for image with clipping effects

The obtained blind estimates for **Method 1** (three block sizes) are collected in Table 6. As it is seen, for 5x5 blocks they are mostly smaller than desired (the lower margin is 0.036), for 7x7 blocks all estimates are within the required limits (from 0.036 to 0.054), and two out of four estimates are larger than desired 0.054) for 9x9 blocks. Thus, 7x7 blocks are again the proper choice for **Method 1**. We would like to stress also that the estimate for the most complex image in Fig. 10(d) is always the largest for any given block size. To our experience, this is due to the influence of image content (large percentage of abnormal local estimates).

Image presented in Figure	Block size		
	5x5	7x7	9x9
10(a)	0.033	0.042	0.043
10(b)	0.034	0.048	0.055
10(c)	0.033	0.045	0.051
10(d)	0.038	0.053	0.061

Table 6. Blind estimates of speckle variance for six-look real-life SAR images obtained by Method 1

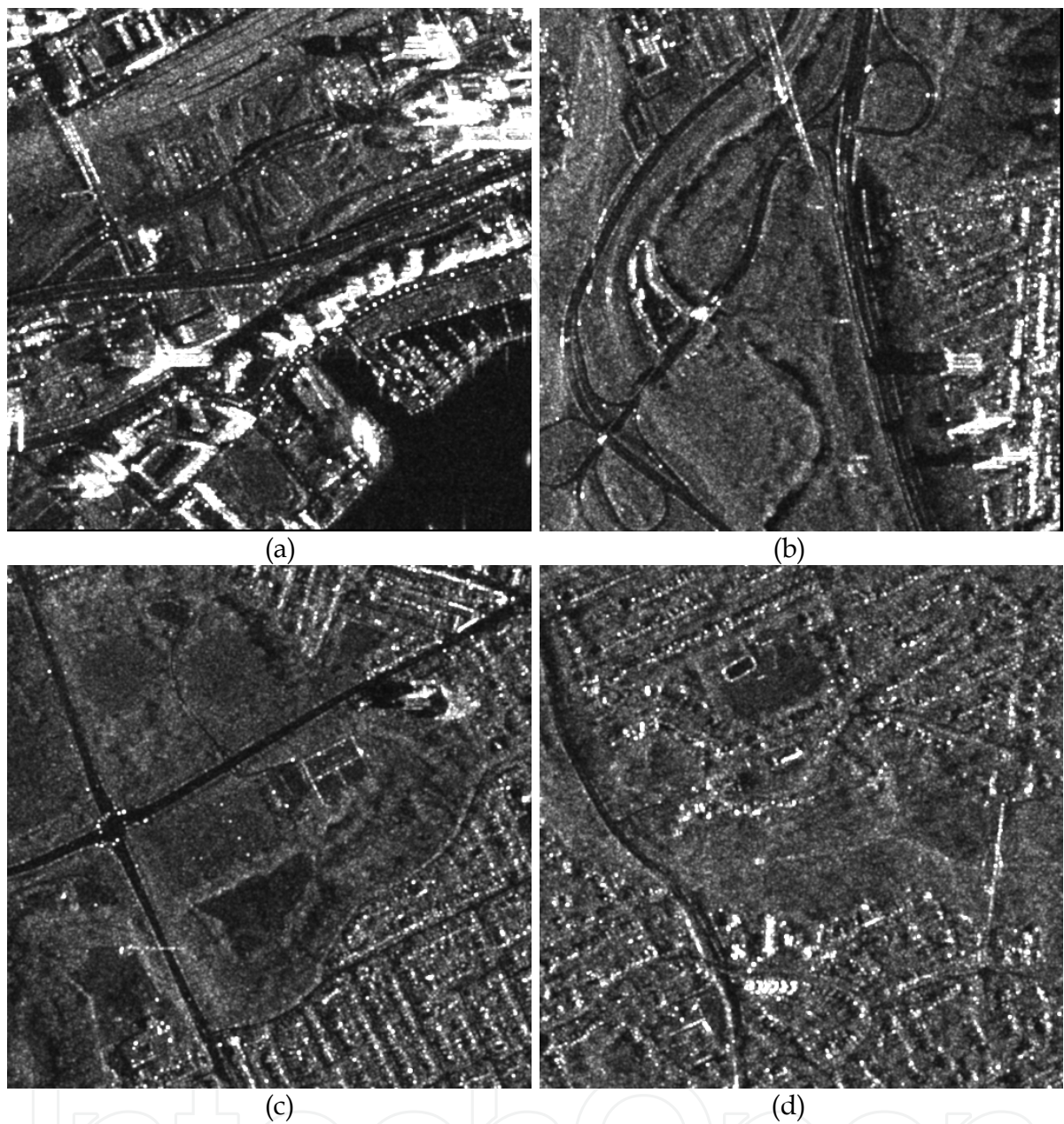


Figure 10. Multi-look SAR elementary images (512x512 pixels) of urban region in Canada

Finally, **Methods 2** and **3** have been verified for six-look images. The estimates are presented in Table 7 for 7x7 blocks. **Method 2** produces obvious overestimation (only one estimate is within the required interval and other ones exceed the upper limit). In turn, **Method 3** provides all four estimates accurate enough although underestimation is observed for all four processed images. Thus, **Method 3** operating in 7x7 blocks provides the best or nearly the best accuracy for all considered simulated and real-life images.

The presented results clearly show that for estimation techniques based on scatter-plots and robust fitting it is often not enough to carry out robust fitting. Image pre-processing able to

partly remove local estimates expected to be abnormal (due to block heterogeneity or to presence of clipping effects) is desirable. Such pre-processing might include image pre-segmentation which in our experiments has been performed by unsupervised variational classification through image multi-thresholding (Klaine et al., 2005). Its advantage is that pre-processing is quite fast. This allows obtaining blind estimates quite quickly since other operations (obtaining of local estimates and robust regression) are also very fast.

Image presented in Figure	Used method	
	Method 2, 7x7 blocks	Method 3, 7x7 blocks
10(a)	0.051	0.041
10(b)	0.061	0.038
10(c)	0.089	0.036
10(d)	0.094	0.044

Table 7. Blind estimates of speckle variance for six-look real-life SAR images obtained by Method 2 and Method 3

5. Conclusions and future work

Some aspects of SAR image simulation have been considered. In particular, it has been stressed that spatial correlation of speckle is to be taken into account. One algorithm to do this is described.

Three methods for blind estimation of noise statistical characteristics in SAR images have been first tested for simulated images. It has been shown that there are several factors influencing their performance. These factors are image content (complexity), the method used and its parameters. It is not always possible to provide blind estimates within desired limits especially for highly textural (complex structure) images. Then, these methods have been verified for real life TerraSAR-X images of limited size of 512x512 pixels. Preliminary tests have clearly demonstrated the presence of essential spatial correlation of speckle, especially for multi-look images. This is taken into account in setting parameters of BENC methods. The block size of 7x7 pixels is recommended for practical use.

The BENC methods based on scatter-plots without image pre-processing produce, on the average, worse accuracy than the method based on mode determination for local estimates' distribution. If pre-processing is applied, BENC methods (as **Method 3**) are able to produce acceptable accuracy for most images. Estimation accuracy for single-look images is mostly acceptable. However, there are more problems with speckle variance estimation for multi-look images. Thus, in future, special attention should be paid to considering multi-look image case. In this sense, the methods based in obtaining noise-informative maps (Uss et al. 2011; Uss et al., 2012) seem to be attractive although they are not so fast as the methods considered above.

This work has been partly supported by French-Ukrainian program Dnipro (PHC DNIPRO 2013, PROJET N° 28370QL).

Author details

Sergey Abramov¹, Victoriya Abramova¹, Vladimir Lukin¹, Nikolay Ponomarenko¹, Benoit Vozel², Kacem Chehdi², Karen Egiazarian³ and Jaakko Astola³

¹ National Aerospace University, Ukraine

² University of Rennes 1, France

³ Tampere University of Technology, Finland

References

- [1] Abramov S., Lukin V., Ponomarenko N., Egiazarian K., & Pogrebnyak O. (2004). Influence of multiplicative noise variance evaluation accuracy on MM-band SLAR image filtering efficiency. *Proceedings of MSMW 2004*, Vol. 1, pp. 250-252, Kharkov, Ukraine, June 2004
- [2] Abramov S., Lukin V., Vozel B., Chehdi K., & Astola J. (2008). Segmentation-based method for blind evaluation of noise variance in images, *Journal of Applied Remote Sensing*, Vol. 2(1), No. 023533, (August 13, 2008), DOI:10.1117/1.2977788
- [3] Abramov S., Zabrodina V., Lukin V., Vozel B., Chehdi K., & Astola J. (2011). Methods for Blind Estimation of the Variance of Mixed Noise and Their Performance Analysis, In: *Numerical Analysis – Theory and Applications*, Ed. J. Awrejcewicz, pp. 49-70, In-Tech, Austria, ISBN 978-953-307-389-7
- [4] Aiazzi B., Alparone L., Barducci A., Baronti S., Marcoinni P., Pippi I., & Selva M. (2006). Noise modelling and estimation of hyperspectral data from airborne imaging spectrometers. *Annals of Geophysics*, Vol. 49, No. 1, February 2006
- [5] Anfinson S.N., Doulgeris A.P., & Eltoft T. (2009). Estimation of the Equivalent Number of Looks in Polarimetric Synthetic Aperture Radar Imagery, *IEEE Transactions on Geoscience and Remote Sensing*, Vol. 47, No. 11, pp. 3795-3809
- [6] Bekhtin Yu. S. (2011). Adaptive Wavelet Codec for Noisy Image Compression, *Proc. of the 9-th East-West Design and Test Symp.*, Sevastopol, Ukraine, Sept., 2011, pp. 184-188
- [7] Choi M.G., Jung J.H., & Jeon J.W. (2009). No-reference Image Quality Assessment Using Blur and Noise, *World Academy of Science, Engineering and Technology*, Vol. 50, pp. 163-167
- [8] Davies E.R. (2000). *Image Processing for the Food Industry*, World Scientific, ISBN 9810240228

- [9] Di Martino G., Poderico M., Poggi G., Riccio D., & Verdoliva L. (2012). SAR Image Simulation for the Assessment of Despeckling Techniques, *Proceedings of IGARSS*, Munich, Germany, July 2012, pp. 1797-1800
- [10] Dogan O., & Kartal M. (2010). Time Domain SAR Raw Data Simulation of Distributed Targets, *EURASIP Journal on Advances in Signal Processing*, Article ID 784815
- [11] DuMouchel W. & O'Brien F. (1989). Integrating a Robust Option into a Multiple Regression Computing Environment in Computing Science and Statistics. *Proc. of the 21st Symposium on the Interface*, pp. 297-301, American Statistical Association, Alexandria, VA
- [12] Egiazarian K., Astola J., Helsingius M., & Kuosmanen P. (1999). Adaptive denoising and lossy compression of images in transform domain. *Journal of Electronic Imaging*, Vol. 8(3), pp. 233-245, DOI:10.1117/1.482673
- [13] Foi A., Trimeche M., Katkovnik V., & Egiazarian K. (2007). Practical Poissonian-Gaussian Noise Modeling and Fitting for Single Image Raw Data. *IEEE Transactions on Image Processing*, Vol. 17, No. 10, pp. 1737-1754
- [14] Foi A. (2009). Clipped Noisy Images: Heteroskedastic Modeling and Practical Denoising. *Signal Processing*, Vol. 89, No. 12, pp. 2609-2629
- [15] Foucher S., Boucher J.-M., & Benie G. B. (2000). Maximum likelihood estimation of the number of looks in SAR images, *Proc. of Int. Conf. Microwave, Radar Wireless Communication*, Wroclaw, Poland, May 2000, Vol. 2, pp. 657-660
- [16] Herrmann J., Faller N., Kern A., & Weber M. (2005). INFOTERRA GMBH Initiatives Commercial Exploitation of TerraSAR-X, *Proc. of ISPRS Hannover Workshop*, Hannover, Germany, May 2005
- [17] Katsaggelos A.K. (Ed.). (1991). *Digital Image Restoration*, Springer-Verlag, New York
- [18] Klaine L., Vozel B., & Chehdi K. (2005). Unsupervised Variational Classification Through Image Multi-Thresholding. *Proc. of the 13th EUSIPCO Conference*, Antalya, Turkey
- [19] Lee J.-S., Hoppel K., & Mango S.A. (1992). Unsupervised Estimation of Speckle Noise in Radar Images, *Int. Journal of Imaging Systems and Technology*. Vol. 4, pp. 298-305
- [20] Lee J.-S., Wen J.H., Ainsworth T.I., Chen K.S., & Chen A.J. (2009). Improved sigma filter for speckle filtering of SAR imagery, *IEEE Transactions on Geoscience and Remote Sensing* Vol. 47(1), pp. 202-213
- [21] Lin C.H., Sun Y.N., & Lin C.J. (2010). A Motion Compounding Technique for Speckle Reduction in Ultrasound Images, *Journal of Digital Imaging*, Vol. 23(3), pp. 246-257
- [22] Liu C., Szeliski R., Kang S.B., Zitnick C.L., & Freeman W.T. (2008). Automatic estimation and removal of noise from a single image. *IEEE Transactions on Pattern Analysis and Machine Intelligence*, Vol. 30, No 2, pp. 299-314

- [23] Lukin V., Abramov S., Zelensky A., Astola J., Vozel B., & Chehdi K. (2007). Improved minimal inter-quantile distance method for blind estimation of noise variance in images, *Proc. SPIE 6748 of Image and Signal Processing for Remote Sensing XIII*, 67481I October 24, 2007, DOI:10.1117/12.738006
- [24] Lukin V., Ponomarenko N., Egiazarian K., & Astola J. (2008). Adaptive DCT-based filtering of images corrupted by spatially correlated noise, *Proc. SPIE 6812 of Image Processing: Algorithms and Systems VI*, 68120W, San Jose, USA, January 2008, DOI: 10.1117/12.764893
- [25] Lukin V., Abramov S., Ponomarenko N., Uss M., Vozel B., Chehdi K., & Astola J. (2009a). Processing of images based on blind evaluation of noise type and characteristics. *Proceedings of SPIE Symposium on Remote Sensing*, Vol. 7477, Berlin, Germany, September 2009
- [26] Lukin V.V., Abramov S.K., Uss M.L., Marusiy I.A., Ponomarenko N.N., Zelensky A.A., Vozel B., & Chehdi K. (2009b). Testing of methods for blind estimation of noise variance on large image database, In: *Practical Aspects of Digital Signal Processing*, Shahty, Russia, Retrieved from <<http://k504.xai.edu.ua/html/prepods/lukin/BookCh1.pdf>>
- [27] Lukin V., Abramov S., Popov A., Eltsov P., Vozel B., & Chehdi K. (2010). A method for automatic blind estimation of additive noise variance in digital images, *Telecommunications and Radio Engineering*, Vol. 69(19), pp. 1681-1702
- [28] Lukin V., Abramov S., Ponomarenko N., Uss M., Zriakhov M., Vozel B., Chehdi K., & Astola J. (2011). Methods and Automatic Procedures for Processing Images Based on Blind Evaluation of Noise Type and Characteristics. *SPIE Journal on Advances in Remote Sensing*, DOI: 10.1117/1.3539768
- [29] Lukin V.V., Abramov S.K., Fevrlev D.V., Ponomarenko N.N., Egiazarian K.O., Astola J.T., Vozel B., & Chehdi K. (2011b). Performance evaluation for Blind Methods of Noise Characteristics Estimation for TerraSAR-X Images, *Proc. SPIE 8180 of Image and Signal Processing for Remote Sensing XVII*, 81800X, Prague, Czech Republic, September 2011, DOI:10.1117/12.897730
- [30] Mallat S. (1998). *A Wavelet tour of signal processing*, Academic Press, San Diego
- [31] Oliver C. & Quegan S. (2004). *Understanding Synthetic Aperture Radar Images*, SciTech Publishing
- [32] Plataniotis K.N. & Venetsanopoulos A.N. (2000). *Color Image Processing and Applications*, Springer-Verlag, NY
- [33] Ponomarenko N.N., Lukin V.V., Egiazarian K.O., & Astola J.T. (2010). A method for blind estimation of spatially correlated noise characteristics, *Proc. SPIE 7532 of Image Processing: Algorithms and Systems VIII*, 753208, San Jose, USA, January 2010, DOI: 10.1117/12.847986

- [34] Ponomarenko N.N., Lukin V.V., & Egiazarian K.O. (2011). Visually Lossless Compression of Synthetic Aperture Radar Images, *Proceedings of ICATT*, Kiev, Ukraine, September 2011, pp. 263-265
- [35] Ramponi G. & D'Alvise R. (1999). Automatic Estimation of the Noise Variance in SAR Images for Use in Speckle Filtering, *Proceedings of IEEE-EURASIP Workshop on Nonlinear Signal and Image Processing*, Vol. 2, pp. 835-838, Antalya, Turkey
- [36] Sendur L. & Selesnick I.W. (2002). Bivariate shrinkage with local variance estimation. *IEEE Signal Processing Letters*, Vol. 9, No. 12, pp. 438-441
- [37] Solbo S. & Eltoft T. (2004). Homomorphic Wavelet-based Statistical Despeckling of SAR Images. *IEEE Trans. on Geosc. and Remote Sensing*, Vol. GRS-42, No. 4, pp. 711-721
- [38] Solbo S. & Eltoft T. (2008). A Stationary Wavelet-Domain Wiener Filter for Correlated Speckle, *IEEE Trans. on Geoscience and Remote Sensing*, Vol. 46(4), pp. 1219-1230
- [39] Touzi R. (2002). A Review of Speckle Filtering in the Context of Estimation Theory. *IEEE Transactions on Geoscience and Remote Sensing*, Vol. 40, No. 11, pp. 2392-2404
- [40] Uss M., Vozel B., Lukin V., & Chehdi K. (2011). Local Signal-Dependent Noise Variance Estimation from Hyperspectral Textural Images. *IEEE Journal of Selected Topics in Signal Processing*, Vol. 5, No. 2, DOI: 10.1109/JSTSP.2010.2104312
- [41] Uss M., Vozel B., Lukin V., & Chehdi K. (2012). Maximum Likelihood Estimation of Spatially Correlated Signal-Dependent Noise in Hyperspectral Images, *Optical Engineering*, Vol. 51, No 11, DOI: 10.1117/1.OE.51.11.111712
- [42] Van Zyl Marais I., Steyn W.H., & du Preez J.A. (2009). On-board image quality assessment for a small low Earth orbit satellite, *Proc. of the 7th IAA Symp. on Small Satellites for Earth Observation*, Berlin, Germany, May 2009
- [43] Vozel B., Abramov S., Chehdi K., Lukin V., Ponomarenko N., Uss M., & Astola J. (2009). Blind methods for noise evaluation in multi-component images, In: *Multivariate Image Processing*, pp. 263-295, France
- [44] Zabrodina V., Abramov S., Lukin V., Astola J., Vozel B., & Chehdi K. (2011). Blind Estimation of mixed noise parameters in images using robust regression curve fitting, *Proc. of 19th European Signal Processing Conference EUSIPCO2011*, Barcelona, Spain, August 2009, pp. 1135 – 1139, ISSN 2076-1465
- [45] Zoran D. & Weiss Y. (2009). Scale Invariance and Noise in Natural Images, *Proc. of IEEE 12th International Conference on Computer Vision ICCV*, Kyoto, Japan, September 2009, pp. 2209-2216, DOI:10.1109/ICCV.2009.5459476

